EuroGNC
Navigation
Guidance — Control
CEAS
Council of European Aerospace Societies

Bristol, UK

June 11th-13th

University of BRISTOL

ROYAL AERONAUTICAL SOCIETY

AIAA

2024

Nonlinear Control Strategy and Sensor Data Processing for a Lift-to-Cruise Aircraft

Denis Surmann   Research Assistant, University of the Bundeswehr Munich, Department of Flight Mechanics and Flight Controls, 85579, Neubiberg, Germany. denis.surmann@unibw.de

Maximilian Weinert   Student, University of the Bundeswehr Munich, Aeronautical Engineering, 85579, Neubiberg, Germany. maximilian.weinert@unibw.de

Stephan Myschik   Professor, University of the Bundeswehr Munich, Department of Flight Mechanics and Flight Controls, 85579, Neubiberg, Germany. stephan.myschik@unibw.de

ABSTRACT

Aerial systems, including electric vertical take-off and landing (eVTOL) vehicles with fixed-wing configurations, present distinct challenges across various flight phases, encompassing hover and the transition to aerodynamic wingborne flight. Effectively addressing these challenges necessitates a robust control framework, prominently featured in the incremental nonlinear dynamic inversion (INDI) approach. However, INDI may encounter constraints like effector saturation and suboptimal pseudoinverses. This paper explores a spectrum of control allocation methods to effectively mitigate these limitations. Additionally, the paper delves into real-world complexities, including sensor noise and stochastic effects. It introduces filtering and estimation techniques to ensure precise data estimations. The proposed methodologies and algorithms undergo rigorous assessment through nonlinear simulations, encompassing comprehensive 6-DOF flight mechanics, realistic sensor models, and the presence of uncertainties. The simulation results underscore the efficacy and applicability of the proposed approaches in addressing the intricate challenges encountered in dynamically controlling eVTOL aircraft with fixed-wing configurations.

Keywords: eVTOL; Nonlinear Controls; Sensor Data Processing

1 Introduction

Aerial systems from aerospace industry has witnessed a paradigm shift towards novel configurations, such as electric vertical take-off and landing (eVTOL) aircraft [1–3]. These vehicles operating for urban air mobility, cargo transport, and various other applications. Realizing this potential, however, necessitates overcoming multifaceted challenges in the design and control of eVTOL platforms. This paper delves into the control system architecture eVTOL development. The operation of the conceptual fixed-wing eVTOL aircraft ranging from hovering to an aerodynamic wingborne flight. Incremental nonlinear dynamic inversion (INDI) approach is applied, which offers a sophisticated framework for dynamic control, enabling these aircraft to seamlessly transition between different flight phases.

The INDI approach fundamentally relies on a rigorous understanding of the underlying mathematics and physics governing the eVTOL flight dynamics. It leverages advanced mathematical techniques to calculate incremental control inputs, allowing for precise adjustments of the vehicle's behaviour. The

complexity of real-world systems introduces challenges that necessitate sensor data processing. This paper shows enhanced filter strategies, aiming to predict and precise data by use of low-pass and complementary filters.

Additional challenges addressed in this paper pertains to the control allocation problem. The eVTOL platforms often feature a surplus of effectors compared to the number of pseudo controls, rendering them over-actuated systems. Managing these excess effectors to optimize control authority while avoiding conflicts and maintaining stability during phase transitions is a formidable task. This paper presents control allocation strategies, including normalization and a redistributed scaled pseudo inverse (RSPI) and constraints via the nullspace transition (NST), to maintain reliable control authority.

The paper is structured as follows: Chapter 2 furnishes general information regarding the conceptual eVTOL aircraft, giving insights into the implementation of flight mechanics utilized in simulations. Additionally, it briefly discusses the flight control architecture. Chapter 3 underscores the primary flight controller, rooted in the principles of INDI. Moreover, it offers detailed insights into design extensions, particularly emphasizing the control allocation task aimed at enhancing control performance. In chapter 4, a linear analysis is presented, focusing on the system robustness amidst uncertainties. Subsequently, nonlinear simulations are showcased, encompassing the primary control performance across all flight phases, alongside an exploration into extended control allocation.

2 Aircraft Representation

This chapter introduces the aircraft configuration of the proposed eVTOL system. It proceeds to delineate the flight control strategy tailored for the designated hardware, encompassing the utilization of sensor data and the deployment of both primary and backup flight control systems. Additionally, it provides a concise overview of the flight mechanics, serving as the foundation for the ensuing nonlinear simulations.

2.1 Aircraft Configuration
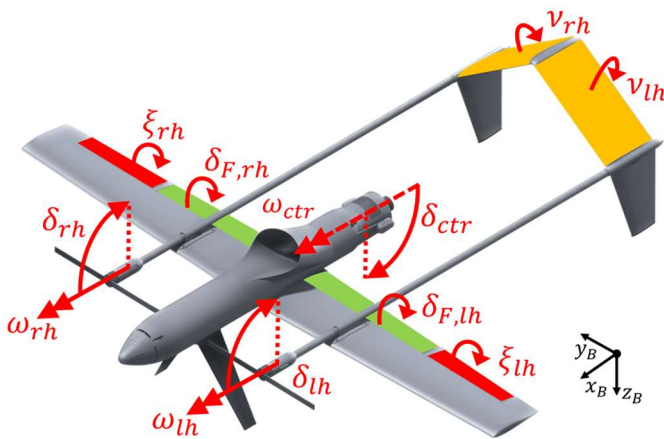
Fig. 1 Pegasus Conceptual Lift-Off and Cruise Vehicle

Table 1 Technical Specifications of Pegasus

Property	Value
Mass m	11 kg
Wingspan b	2.10 m
Wing area S	0.952 m^2
Length l	2.04 m
Number of impellers	1
Number of propellers	2

The Pegasus project introduces a conceptual electric vertical take-off and landing (eVTOL) aircraft, as depicted in Fig. 1 and detailed in Table 1. This aircraft features a fixed-wing configuration with a wingspan of 2.1 meters and is equipped with an electric propulsion system consisting of two propellers and one impeller. Pegasus has been designed for observation missions, housing a thermal and optical camera system on board.

The vehicle incorporates two propellers and one impeller, each characterized by their respective rotational speeds denoted as ω_{lh}, ω_{rh}, and ω_{ctr}. Each propulsion unit is capable of altering its thrust vector through deflection, with the central propulsion deflection, δ_{ctr}, capable of rotating up to a 90° angle. In contrast, the propeller deflections, δ_{lh} and δ_{rh}, can vary between 0° and 105°, allowing for hovering flight. In this context, hovering refers to the aircraft's ability to counteract gravitational forces using the available thrust directions and forces. Yaw and roll axis control is primarily achieved through the two propellers, while pitch control involves interaction between all propulsion units.

During wingborne flight, the lift generated by the wings effectively offsets the aircraft's weight, and aerodynamic control surfaces enable precise control over moments. Pitch and yaw control are accomplished by deflecting the ruddervator ν_{lh} and ν_{rh}, while roll control is achieved by deflecting the ailerons ξ_{lh} and ξ_{rh}. Wingborne flight occurs at airspeeds above the stall speed, which can be reduced to 15 m/s using the flaps $\delta_{F,lh}$ and $\delta_{F,rh}$.

Throughout the phases of acceleration and deceleration, the contribution of the aerodynamic surfaces to counterbalance gravitational forces, as well as the effectiveness of the aerodynamic control surfaces, varies. The transition phase extends from hovering to above stall speed. The cruising speed of the aircraft is 30 m/s and can be achieved either by utilizing the propellers or the impeller. In observation scenarios with lower airspeed requirements, using the propellers may extend the flight time.

2.2 Flight Control System Architecture

The flight control system architecture is comprised of two flight control computers (FCCs), as illustrated in Fig. 2 comparable to the architecture as shown in [4]. This system includes a primary and a backup FCC, an automation component responsible for overall system management and a voting element selecting the actuator / motor commands.
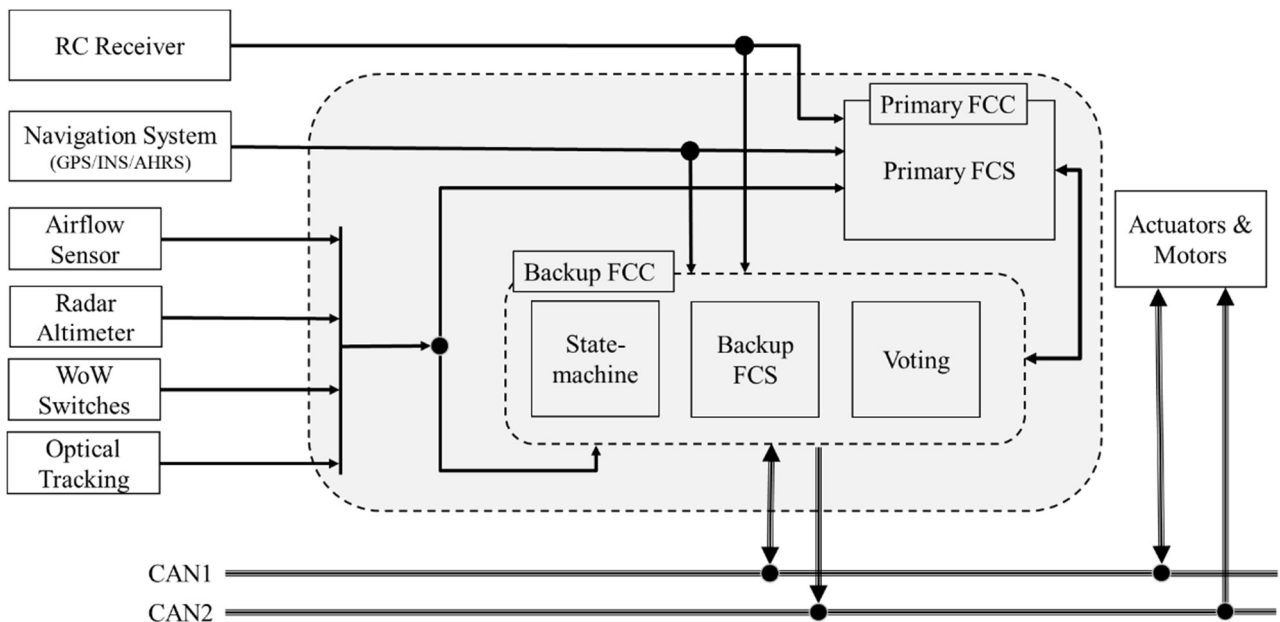
Fig. 2 Architecture of the Flight Control Computer

Fig. 2 also highlights the main sensor components required for vehicle operation. A tactical grade navigation system provides position, velocity, and vehicle attitude as well as acceleration and rotational rates required for the primary flight control algorithm. An airflow sensor is used to obtain additional

information about the current aerodynamic inflow as well as wind information. For indoor operation, an optical tracking system can also be incorporated into the system.

Additionally, sensors like weight-on-wheels (WoW) sensors and a radar altimeter, primarily active during landing and near ground operations, complement the navigation suite.

In this paper, we specifically emphasize the primary FCC and the navigation system sensors incorporated into our simulation framework. Hardware selection aligns with envisioned control philosophies and is validated through hardware-in-the-loop (HIL) testing. The primary FCS operates using the incremental nonlinear dynamic inversion method, elaborated upon in this paper. The backup controller, although not the focus of this research paper, is developed with the aim of relying on a minimum number of sensor information, providing capabilities to safely land the vehicle. As of now, several different control philosophies are under investigation, including a nonlinear dynamic inversion (NDI) approach, known for its effectiveness in mitigating actuator saturations [5,6].

2.3 Flight Mechanic Representation

The aircraft is mathematically represented within a framework of nonlinear system dynamics characterized by input non-affinity and time invariance. The nonlinear equations of motion governing the six degrees of freedom (6-DOF) for rigid body motion are considered, accounting for the curvature and rotation of the Earth as well as an arbitrary reference point denoted as R. These equations are described as follows, with Eq. (1) handling translational motion and Eq. (2) addressing rotational motion [7–9]:

$$\left(\dot{V}_K^R\right)_B^{EB} = \frac{(F_T^R)_B}{m} - (\omega_K^{EB})_B \times (V_K^R)_B^E - 2 \cdot (\omega_K^{IE})_B \times (V_K^R)_B^E - (\omega_K^{IE})_B \times [(\omega_K^{IE})_B \times (r^G)_B] \tag{1}$$

$$-(\dot{\omega}_K^{IB})_B^B \times (r^{RG})_B - (\omega_K^{IB})_B \times [(\omega_K^{EB})_B \times (r^{RG})_B],$$

$$\left(\dot{\omega}_K^{IB}\right)_B^B = (I^R)_{BB}^{-1} \cdot [(M_T^R)_B - (\omega_K^{IB}) \times [(I^R)_{BB} \cdot (\omega_K^{IB})_B] - \tag{2}$$

$$m \cdot (r^{RG})_B \times \left[\left(\dot{V}_K^R\right)_B^{IB} + (\omega_K^{IB})_B \times (V_K^R)_B^I\right]\right].$$

The superscript/index E denotes the Earth-Centered-Earth-Fixed system, B is referring to the body-fixed system and I to the Earth-centered inertial system. The angular velocity and acceleration are given by ω and $\dot{\omega}$, the kinematic velocity and acceleration of the reference point R are given by $(V_K^R)_B^E$ and $\left(\dot{V}_K^R\right)_B^{EB}$, the moments of inertia are described by $(I^R)_{BB}$ and m represents the mass of the vehicle.

The total forces and moments, expressed in Eq. (3) and (4), are modelled as the sum of contributions from aerodynamics (A), propulsion (P), and gravity (G):

$$(F_T^R)_B = (F_P^R)_B + (F_A^R)_B + (F_G^R)_B, \tag{3}$$

$$(M_T^R)_B = (M_P^R)_B + (M_A^R)_B + (M_G^R)_B, \tag{4}$$

Aerodynamic forces are given as

$$(F_A^A)_A = \begin{bmatrix} X_A^A \\ Y_A^A \\ Z_A^A \end{bmatrix}_A = \begin{bmatrix} -D \\ Q \\ -L \end{bmatrix}_A = \frac{1}{2}\rho V_A^2 S \begin{bmatrix} -C_D \\ C_Q \\ -C_L \end{bmatrix}_A \; ; (F_A^R)_B = \mathbf{M}_{BA}(F_A^A)_A, \tag{5}$$

with L denoting the lift, D is drag, and Q denotes the cross-stream force in the aerodynamic frame A. V_A represents airspeed, ρ stands for air density, S represents wing area, and C signifies aerodynamic coefficients. These coefficients are described using Taylor series expansion [10]. The transformation from A to B-frame is achieved using the matrix $\mathbf{M}_{BA}$. Aerodynamic moments are outlined as:

$$(M_A^A)_B = \begin{bmatrix} L_A^A \\ M_A^A \\ N_A^A \end{bmatrix}_B = \frac{1}{2}\rho V_A^2 S \begin{bmatrix} sC_l \\ \bar{c}C_m \\ sC_n \end{bmatrix}_B \; ; \; (M_A^R)_B = (M_A^A)_B + (r^{RA})_B \times (F_A^A)_B \tag{6}$$

with $\bar{c}$ being the mean aerodynamic chord, s denoting the semi wingspan, and $(r^{RA})_B$ symbolizing the distance between the aerodynamics reference point A and the reference point R. In hover, the aerodynamic forces are characterized by corresponding flat plate coefficients. A blending κ with respect to the airspeed is used to consider wingborne (wb) and hover (ho) coefficients [11]:

$$\begin{bmatrix} C_D \\ C_Q \\ C_L \end{bmatrix} = (1-\kappa)\begin{bmatrix} C_D \\ C_Q \\ C_L \end{bmatrix}_{ho} + \kappa\begin{bmatrix} C_D \\ C_Q \\ C_L \end{bmatrix}_{wb} , \tag{7}$$

$$\begin{bmatrix} C_l \\ C_m \\ C_n \end{bmatrix} = \kappa\begin{bmatrix} C_l \\ C_m \\ C_n \end{bmatrix}_{wb} . \tag{8}$$

The blending parameter κ is determined using a sigmoid function to smoothly transition between hover and wingborne characteristics. Gravity contribution is expressed in Eq. (9).

$$(F_G^G)_B = \begin{bmatrix} X_G^G \\ Y_G^G \\ Z_G^G \end{bmatrix}_B = \begin{bmatrix} -\sin\Theta \\ \sin\Phi\cos\Theta \\ \cos\Phi\sin\Theta \end{bmatrix} mg, \tag{9}$$

with the bank angle Φ, the pitch angle Θ and the gravitational acceleration constant g. The gravitational force acts on the centre of gravity G, and when represented at reference point R, it generates an additional moment.

$$(M_G^R)_B = (r^{RG})_B \times (F_G^G)_B. \tag{10}$$

The propulsion contributions depend on thrust levels and deflection angles of each propulsion so that forces F_P and moments M_P can be expressed as:

$$(F_P^R)_B = \begin{bmatrix} \sum T_i \cos\delta_i \\ 0 \\ -\sum T_i \sin\delta_i \end{bmatrix}, \tag{11}$$

$$(M_P^R)_B = \sum (r^{RP_{f_i}})_B \times (F_{P_i}^R)_B, \tag{12}$$

with index i for each propulsion and $r^{RP_{f_i}}$, which defines the vector between the reference point and the propulsion frame. The forces in Eq. (11) are based on the chosen motor and blade components that are currently available by theoretical investigation. Future work will include more detailed experimental investigations to confirm the data sheet references which are pointed out in Table 2.

Thrust of each propulsor is generated with the diameter d and the thrust coefficient is defined by c_T [12]:

Table 2 Performance Characteristics of the Propulsion System

Engines	Impeller	Propeller
Diameter d	0.12 m	0.41 m
Max Thrust T_{max}	86 N	49 N
Max Rotational Speed ω_{max}	3142 rad/s	955 rad/s
Thrust Coefficient c_T	1.35	0.064
Engine Time Constants T	0.01 s	0.01 s

$$T = (2\pi\omega)^2 \rho d^4 c_T. \tag{13}$$

3 Flight Control System

In this chapter, the core structure of the INDI implementation with extensions is presented.

3.1 Controller Structure

This chapter provides fundamental explanations regarding the INDI control structure depicted in Fig. 3, with the reference model (RM), error controller (EC), control allocation (CA), on-board plant model (OBPM), and command mapping (CM). The Estimator ($\widehat{E}$) will be discussed later as part of the sensor data processing.
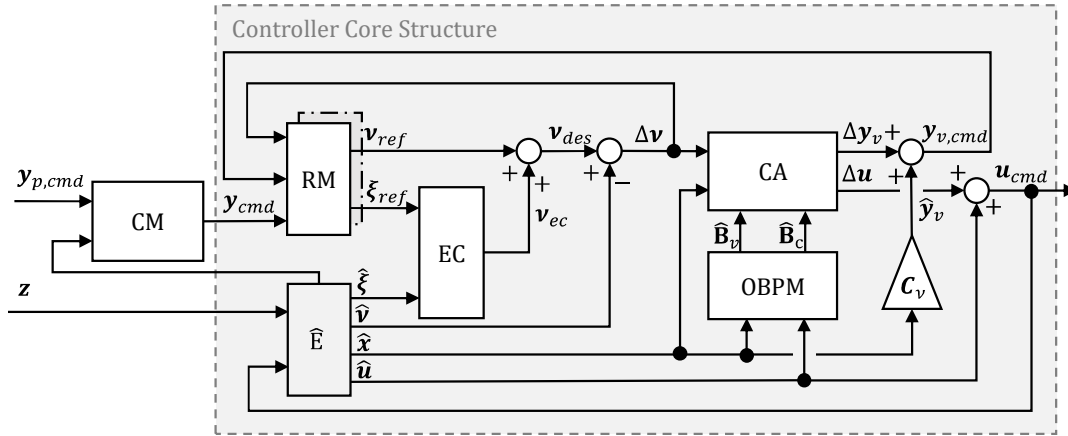

Fig. 3 Assembly of the Controller [13]

3.1.1 Command Mapping and Reference Model

The CM generates the pilot inputs for the RM with

$$\boldsymbol{y}_{p,cmd} = \begin{bmatrix} (u_K^G)_C^E \\ (v_K^G)_C^E \\ (w_K^G)_C^E \\ \dot{\Psi} \end{bmatrix}_{cmd} . \tag{14}$$

Eq. (14) comprises the kinematic velocity components $(u_K^G)_C^E, (v_K^G)_C^E, (w_K^G)_C^E$ with respect to Earth in the Control-frame (C-frame) and the derivative of the Euler angle $\dot{\Psi}$. The C-frame is rotated by the azimuth angle in comparison to the North-East-Down-System and ensure an intuitive interface in the whole flight envelope [14]. The RM, driven by inputs from the CM, generates desired trajectories using two decoupled models: an outer loop for velocity and an inner loop for attitude. Pseudo controls are chosen as:

$$\boldsymbol{v}_{ref} = \begin{bmatrix} \boldsymbol{n}_C \\ \dot{\boldsymbol{\omega}} \end{bmatrix}_{ref}, \tag{15}$$

where $\boldsymbol{n}_C \in \mathbb{R}^3$ represents load factors in the Control-frame and $\dot{\boldsymbol{\omega}} \in \mathbb{R}^3$ represents body angular accelerations. The velocity loop RM is considered a first-order model with a relative degree of 1, while the attitude loop RM computes body angular acceleration using the strap-down equation, implying a relative degree of 2 [15]. The outer loop results in an allocation within the CA, producing virtual control inputs (VCIs):

$$\boldsymbol{y}_{v,cmd} = \begin{bmatrix} \Phi \\ \Theta \end{bmatrix}_{v,cmd} . \tag{16}$$

These VCIs, Φ with the bank angle and Θ as the pitch angle, remain the same during all flight phases and prevent a use of mode switches.

3.1.2 Error Controller

The EC is a simple P control to regulate the error trajectory with

$$\boldsymbol{v}_{ec} = \boldsymbol{K}_P(\boldsymbol{\xi}_{ref} - \hat{\boldsymbol{\xi}}), \tag{17}$$

where $\boldsymbol{v}_{ec}$ is the error controller pseudo control, $\boldsymbol{K}_P$ is the proportional gain, $\boldsymbol{\xi}_{ref}$ are the external states from the RM and $\hat{\boldsymbol{\xi}}$ the estimated states from the estimator. The choice of the P-gain impacts the controller's performance and must be designed accordingly [16].

3.1.3 On-Board Plant Model

The plant dynamics are represented within the OBPM, which considers estimated aircraft and actuator states. The OBPM continuously updates Jacobian matrices as the output with respect to the input:

$$\hat{\mathbf{B}}_v = \frac{\partial \hat{\boldsymbol{v}}}{\partial \hat{\boldsymbol{u}}}, \tag{18}$$

$$\hat{\mathbf{B}}_c = \frac{\partial \hat{\boldsymbol{c}}}{\partial \hat{\boldsymbol{u}}}. \tag{19}$$

The matrices $\hat{\mathbf{B}}_v$ and $\hat{\mathbf{B}}_c$ represent effectiveness matrices for the actuators and the virtual control inputs and the defined constraints that are used in the CA [17]. Both matrices are updated at each sample time due to perturbations applied to the estimated inputs $\hat{\boldsymbol{u}}$.

3.1.4 Control Allocation

The CA computes incremental controls using a common pseudoinverse, as referenced in the literature [18]:

$$\Delta \boldsymbol{u} = \hat{\mathbf{B}}_v^+ \Delta \boldsymbol{v}_{des}, \tag{20}$$

with the pseudo inverse $\hat{\mathbf{B}}_v^+$ of matrix $\hat{\mathbf{B}}_v$, denoted with a "+". This is the fundamental understanding of incremental nonlinear dynamic inversion [19–21]. The conceptual eVTOL aircraft is equipped with 14 effectors that manage six pseudo controls. Consequently, the vehicle operates as an over-actuated system. It's important to note that the aircraft has 12 inherent effectors, but an additional two are introduced if the virtual control inputs (VCIs) described in Eq. (16) are also considered. The number of active effectors varies during different flight phases, as outlined in Table 3. This necessitates efficient utilization of available control elements for each flight phase. However, it also implies the maximum utilization of effectors during the transition phase, maintaining the status of an over-actuated system throughout all flight phases.

Table 3 Active Effectors during different Flight Phases

	ω_{ctr}	ω_{lh}	ω_{rh}	δ_{ctr}	δ_{lh}	δ_{rh}	ξ_{lh}	ξ_{rh}	$\delta_{F,lh}$	$\delta_{F,rh}$	v_{lh}	v_{rh}	Φ	Θ	Σ
Hover	x	x	x	x	x	x							x	x	8
Transition	x	x	x	x	x	x	x	x	x	x	x	x	x	x	14
Wingborne	x	(x)	(x)				x	x	x	x	x	x	x	x	9(11)

3.2 Nullspace Transition (NST)

Addressing the challenge posed by an over-actuated system, the INDI approach may introduce path dependencies due to its inherent integrating property [19]. This can lead to internal conflicts and reduced control effectiveness over time. To mitigate these issues, constraints are introduced and expressed in Eq. (19). As an illustrative example, consider the behaviour related to the pitch angle Θ. When the aircraft is accelerating in hover, two potential solutions exist: reducing Θ or decreasing the deflections of the propellers and impeller. In the first scenario, additional acceleration could result in a negative angle of attack, which could have catastrophic consequences in case of any malfunction. However, adjusting the deflections of the motors can maintain a positive or neutral angle of attack, keeping the pitch above 0°. Therefore, a nullspace transition (NST) is implemented to align with the control philosophy and utilize constraints effectively. The NST relies in the nullspace of $\widehat{\mathbf{B}}_v$ and computes additional control increments. Consider the case of an incremental NST input which is given by:

$$\Delta \boldsymbol{u}_{NST} = \mathbf{N}_{\widehat{\mathbf{B}}_v} \boldsymbol{k}_{NST}, \tag{21}$$

with $\mathbf{N}_{\widehat{\mathbf{B}}_v}$ representing the nullspace of the effectiveness matrix $\widehat{\mathbf{B}}_v$. And thus $\Delta \boldsymbol{u}_{NST}$ lies in the nullspace of $\widehat{\mathbf{B}}_v$. The vector $\boldsymbol{k}_{NST}$ can be selected arbitrary for this purpose. The control command can be expanded such that:

$$\Delta \boldsymbol{u} = \Delta \boldsymbol{u}_{PI} + \Delta \boldsymbol{u}_{NST}, \tag{22}$$

that accounts for the solution of the pseudoinverse from Eq. (20) and the incremental input from Eq. (21). This means that

$$\Delta \boldsymbol{u} = \Delta \boldsymbol{u}_{PI} + \mathbf{N}_{\widehat{\mathbf{B}}_v} \boldsymbol{k}_{NST}. \tag{23}$$

The constraints $\boldsymbol{c}$ are introduced by

$$\Delta \hat{\boldsymbol{c}} = \widehat{\mathbf{B}}_c \big(\Delta \boldsymbol{u}_{PI} + \mathbf{N}_{\widehat{\mathbf{B}}_v} \boldsymbol{k}_{NST} \big), \tag{24}$$

$$\Delta \hat{\boldsymbol{c}} = \mathbf{0} - \hat{\boldsymbol{c}} = -\hat{\boldsymbol{c}}, \tag{25}$$

with $\hat{\boldsymbol{c}}$ from the estimation of the OBPM from the current measurements. Inserting Eq. (24) in Eq. (25) formulates

$$-\hat{\boldsymbol{c}} = \widehat{\mathbf{B}}_c \big(\Delta \boldsymbol{u}_{PI} + \mathbf{N}_{\widehat{\mathbf{B}}_v} \boldsymbol{k}_{NST} \big), \tag{26}$$

The NST builds additional input increments but is not affecting the pseudo controls [22,13,23], so that the reformulation is:

$$\Delta \boldsymbol{u}_{NST} = -\mathbf{N}_{\widehat{\mathbf{B}}_c} \big[\widehat{\mathbf{B}}_c \mathbf{N}_{\widehat{\mathbf{B}}_c} \big]^+ \big(\widehat{\mathbf{B}}_c \Delta \boldsymbol{u}_{PI} + \hat{\boldsymbol{c}} \big), \tag{27}$$

considering Eq. (21) and Eq. (26). Finally, a summation of $\Delta \boldsymbol{u}_{PI}$ and $\Delta \boldsymbol{u}_{NST}$ in Eq. (22) results in the incremental command from the INDI control. The chosen constraints vary with respect to the number of effectors and the desired control philosophy. For this aircraft, the following constraints are implemented:

$$\hat{c}_1 = \left(\frac{\widehat{\Theta} - 5 \frac{\pi}{180} \lambda}{\Theta_{max}} \right)^2 (1 - \lambda), \tag{28}$$

$$\hat{c}_2 = \left[\left(\frac{\hat{\xi}_{lh}}{\xi_{max}} \right)^2 + \left(\frac{\hat{\xi}_{rh}}{\xi_{max}} \right)^2 \right] (1 - \lambda), \tag{29}$$

$$\hat{c}_3 = \left[\left(\frac{\hat{v}_{lh}}{v_{max}}\right)^2 + \left(\frac{\hat{v}_{rh}}{v_{max}}\right)^2\right](1 - \lambda),\tag{30}$$

$$\hat{c}_4 = \begin{cases} \left(\frac{\hat{\delta}_{F,lh} - 5\frac{\pi}{180}}{\delta_{F,max}}\right)^2 + \left(\frac{\hat{\delta}_{F,rh} - 5\frac{\pi}{180}}{\delta_{F,max}}\right)^2, & 0 \leq \lambda < 1 \\[2em] \left(\frac{\hat{\delta}_{F,lh}}{\delta_{F,max}}\right)^2 + \left(\frac{\hat{\delta}_{F,rh}}{\delta_{F,max}}\right)^2, & \lambda = 1 \end{cases}\tag{31}$$

$$\hat{c}_5 = \left[\left(\frac{\hat{v}_{lh}}{v_{max}}\right)^2 - \left(\frac{\hat{v}_{rh}}{v_{max}}\right)^2\right]\lambda,\tag{32}$$

$$\hat{c}_6 = \left(\frac{\hat{\delta}_{F,lh}}{\delta_{F,max}}\right)^2 - \left(\frac{\hat{\delta}_{F,rh}}{\delta_{F,max}}\right)^2,\tag{33}$$

$$\hat{c}_7 = \left[\left(\frac{\hat{\omega}_{lh}}{\omega_{lh,max}}\right)^2 + \left(\frac{\hat{\omega}_{rh}}{\omega_{rh,max}}\right)^2\right]\lambda,\tag{34}$$

$$\hat{c}_8 = \begin{cases} \left[\left(\frac{\hat{\delta}_{ctr}}{\delta_{ctr,max}}\right)^2 + \left(\frac{\hat{\delta}_{lh}}{\delta_{lh,max}}\right)^2 + \left(\frac{\hat{\delta}_{rh}}{\delta_{rh,max}}\right)^2\right]\lambda, & 0 < \lambda \leq 1 \\[2em] \left[\left(\frac{\hat{\delta}_{ctr} - \frac{\pi}{2}}{\delta_{ctr,max}}\right)^2 + \left(\frac{\hat{\delta}_{lh} - \frac{\pi}{2}}{\delta_{lh,max}}\right)^2 + \left(\frac{\hat{\delta}_{rh} - \frac{\pi}{2}}{\delta_{rh,max}}\right)^2\right], & \lambda = 0 \end{cases}\tag{35}$$

1) Constraint 1, as denoted in Eq. (28), mandates the aircraft to uphold a pitch angle of zero degrees during hover. However, a slight decrement to up to five degrees is warranted during the transition phase. This strategy ensures a positive angle of attack, thereby consistently generating positive lift. Furthermore, it aligns the CA mechanism to direct acceleration towards the propulsion deflections. Consequently, the aircraft achieves acceleration devoid of the pitch-down behaviour typically associated with multicopters.

2) Constraints 2 to 4, outlined in Eq. (29) to (31), address the reduction of aerodynamic surface utilization in low-speed flight regimes. The flaps are constrained to five degrees. As speed decreases, the effectiveness of these surfaces diminishes, as reflected in the effectiveness matrix by small elements. Consequently, this interaction precipitates substantial increments in the control output to compensate for the reduced effectiveness of aerodynamic surfaces.

3) Constraints 5 to 6, as articulated in Eq. (32) and (33), presuppose symmetrical deflections of the ailerons and ruddervators. Notably, the symmetrical deflections of the ruddervators serve to preclude the CA system from utilizing them for roll moment generation.

4) Constraints 7 to 8, detailed in Eq. (34) to (35) manage the behaviour of the propulsion systems across various flight phases. During the transition to wingborne flight, the propellers are commanded to decelerate gradually until reaching zero speed. Concurrently, the tilt mechanism deflections are constrained to maintain a straightforward position of zero degrees in the wingborne and with deflections of 90 degrees in hover.

Note that the blending factor λ transitions from zero during hover to one during wingborne flight in accordance with the aircraft velocity.

3.3 Normalization and Redistributed Scaled Pseudo Inverse

In general cases, the incremental input vector approaches with Eq. (20). However, the original approach fails to account for several critical factors:

1) The effectiveness matrix does not consider the varying effectiveness of each effector within their specified minimum and maximum operational bounds.
2) The incremental solution, Δu, does not incorporate any form of saturation. Saturation can arise due to actuator limitations or physical constraints of the aircraft, resulting in the failure to achieve the desired pseudo controls.

A solution to these issues is provided through a process of normalization and the application of a Redistributed Scaled Pseudo Inverse (RSPI), depicted in Fig. 4 for reference in the following sections [22,23].
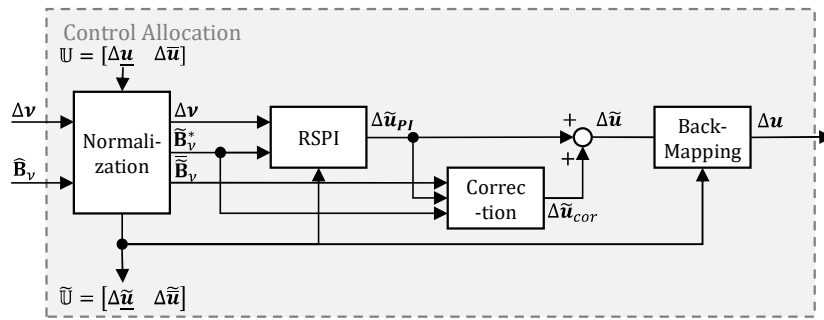

Fig. 4 Normalization and RSPI in the CA

3.3.1 Normalization

In Eq. (20), the control subset $\mathbb{U}$ operates within an n-dimensional space with different lengths in each direction. $\widehat{\mathbf{B}}_v$ is not considering the effectors with their operational ranges. To illustrate, consider the impeller and an aerodynamic surface: while the impeller's rotational speed can range from 0 to 3000 rad/s, the aerodynamic surface may have a range of $\pm\pi/6$. Consequently, a small entry in the effectiveness matrix may lead to disproportionately large incremental solutions when applying the pseudoinverse from Eq. (20). In some flight phases, the impeller may be more effective than the aerodynamic surface, especially at lower airspeeds. To address this, the subspace $\mathbb{U}$ can be normed to the $\widetilde{\mathbb{U}}$-space. In the following, normed values are characterized by $'\sim'$. If

$$\Delta\widetilde{u} = \mathbf{W}\Delta u,\tag{36}$$

and

$$\mathbf{W} = diag\left(\frac{2}{\Delta\overline{u}_i - \Delta\underline{u}_i}\right),\tag{37}$$

the upper and lower normed incremental boundaries become

$$\Delta\widetilde{\underline{u}} = -[1 \dots 1]^T,\tag{38}$$
$$\Delta\widetilde{\overline{u}} = [1 \dots 1]^T.$$

In Eq. (37), $\Delta\overline{u}_i$ and $\Delta\underline{u}_i$ represent the upper or lower incremental saturation. This saturation occurs to the effector speed $\dot{\overline{u}}, \dot{\underline{u}}$ by every time step or absolute boundaries which decrease the incremental limits by $\overline{u} - u_0$ or $\underline{u} - u_0$ for the upper or lower saturations. Now taking Eq. (36) and insert into the basic INDI formulation in Eq. (20), following expression can be made [23]:

$$\Delta \boldsymbol{v}_{des} = \widehat{\mathbf{B}}_v \mathbf{W}^{-1} \Delta \widetilde{\boldsymbol{u}} = \widetilde{\mathbf{B}}_v \Delta \widetilde{\boldsymbol{u}}, \tag{39}$$

$$\Delta \boldsymbol{u} = \mathbf{W}^{-1} \Delta \widetilde{\boldsymbol{u}}.$$

With this, we achieve normalization into the control subspace $\widetilde{\mathbb{U}}$ with the first aspect, but also the back-mapping of the incremental control vector solution into $\mathbb{U}$-space. These methods encompass both the input and output aspects of the scheme depicted in Fig. 4. In some cases, the effectiveness matrix may need to be adjusted, assuming that the effectors' impact on the pseudo controls is minimal. In other situations, certain portions of the effectiveness matrix may need to be cancelled to prevent ineffective solutions. The relationship between the modified $\widetilde{\mathbf{B}}_v^*$-matrix and the original $\widetilde{\mathbf{B}}_v$-matrix is described as follows:

$$\widetilde{\mathbf{B}}_v = \widetilde{\mathbf{B}}_v^* + \overline{\overline{\mathbf{B}}}_v. \tag{40}$$

As demonstrated in [22], manipulation of $\mathbf{B}$ results in divergence between the achieved ('*ach*') and the desired ('*des*') pseudo controls: $\Delta \boldsymbol{v}_{ach} \neq \Delta \boldsymbol{v}_{des}$. The correction can be done by:

$$\Delta \boldsymbol{v}_{ach} = \Delta \boldsymbol{v}_{des} = \widetilde{\mathbf{B}}_v^* (\Delta \widetilde{\boldsymbol{u}}_{PI} + \Delta \widetilde{\boldsymbol{u}}_{cor}) + \overline{\overline{\mathbf{B}}}_v (\Delta \widetilde{\boldsymbol{u}}_{PI} + \Delta \widetilde{\boldsymbol{u}}_{cor}). \tag{41}$$

There is an infinite number of solutions for the non-square matrices $\widetilde{\mathbf{B}}_v^*$ and $\overline{\overline{\mathbf{B}}}_v$ that account for the correction $\Delta \widetilde{\boldsymbol{u}}_{cor}$. Like presented with the NST, there is one solution for the correction that lies within the nullspace of $\overline{\overline{\mathbf{B}}}_v$ [22].

$$\Delta \widetilde{\boldsymbol{u}}_{cor} = \mathbf{N}_{\overline{\overline{\mathbf{B}}}} \boldsymbol{k} \tag{42}$$

$$\widetilde{\mathbf{B}}_v^* \mathbf{N}_{\overline{\overline{\mathbf{B}}}} \boldsymbol{k} + \overline{\overline{\mathbf{B}}}_v \Delta \widetilde{\boldsymbol{u}}_{PI} = 0 \tag{43}$$

$$\Delta \widetilde{\boldsymbol{u}}_{cor} = -\mathbf{N}_{\overline{\overline{\mathbf{B}}}} \left[\widetilde{\mathbf{B}}_v^* \mathbf{N}_{\overline{\overline{\mathbf{B}}}} \right]^+ \overline{\overline{\mathbf{B}}}_v \Delta \widetilde{\boldsymbol{u}}_{PI} \tag{44}$$

Eq. (43) ensures that the desired pseudo control remains unaffected and reaches the desired value. Eq. (44) is expressed by Eq. (42)-(43) that implicates the correction control vector.

3.3.2 Redistributed Scaled Pseudo Inverse

Each effector operates with its specific dynamics within the controller's sample time. If a solution leads to the saturation of the incremental control vector, indicating that the desired pseudo control has not been achieved, an effective approach is the Redistributed Scaled Pseudo Inverse (RSPI) [22,23], illustrated in Fig. 5. This method allocates the solution while considering the physical limitations. With the remaining control authority, the residual pseudo controls may be reached in additional iterations.

In the first step, the control allocation allocates the solution of the incremental control vector as $\Delta \widetilde{\boldsymbol{u}}^1 = \left(\widetilde{\mathbf{B}}_v^1 \right)^+ \Delta \boldsymbol{v}_{des}^1$ with index 1. After confirming the solution with respect to the boundaries of the incremental control vector, scaling is applied as follows:
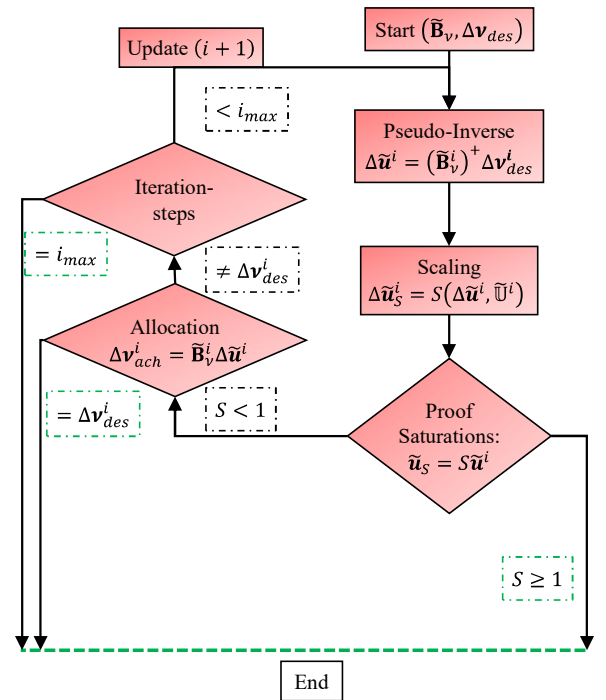
Fig. 5 Sequence of the Redistributed Scaled Pseudo Inverse [24]

$$\tilde{\pmb{u}}_S = S(\tilde{\pmb{u}}, \mathbb{U}) = \left(\min\left\{1, \frac{g(\tilde{u}_i)}{\tilde{u}_i}\right\}\right)\tilde{\pmb{u}}, i = 1 \dots m, \tag{45}$$

with the scaling factor S and $g(\tilde{u}_i)$ representing the minimum or maximum available increment of every effector:

$$g(\tilde{u}_i) = \begin{cases} \Delta\underline{\tilde{u}}_i, & \tilde{u}_i < 0 \\ \Delta\overline{\tilde{u}}_i, & \tilde{u}_i > 0 \end{cases}. \tag{46}$$

When S equals one, it implies that the effector is not saturated, and thus, the desired pseudo control is achieved. If at least one element saturates in $\Delta\tilde{\pmb{u}}^1$, the scaling factor becomes less than 1, and the index 1 solution is scaled with $\Delta\tilde{\pmb{u}}_S^1 = S(\Delta\tilde{\pmb{u}}^1, \mathbb{U})$. The achieved pseudo controls can be computed by modifying Eq. (20) so that the first achieved pseudo controls are given by:

$$\Delta\pmb{v}_{ach}^1 = \widetilde{\pmb{B}}_v^1 \Delta\tilde{\pmb{u}}_S^1. \tag{47}$$

For the second iteration, the residual pseudo controls are determined as:

$$\Delta\pmb{v}_{des}^2 = \Delta\pmb{v}_{des}^1 - \Delta\pmb{v}_{ach}^1. \tag{48}$$

Before the second iteration begins, columns corresponding to saturated effectors are eliminated from $\widetilde{\pmb{B}}_v^1$, resulting in an updated effectiveness matrix, $\widetilde{\pmb{B}}_v^2$. With this updated matrix, the saturated effectors no longer affect the subsequent iterations. The second iteration hence starts with $\Delta\tilde{\pmb{u}}^2 = (\widetilde{\pmb{B}}_v^2)^+\Delta\pmb{v}_{des}^2$.

The RSPI process continues until either the desired pseudo controls are reached, or all effectors are saturated. The solution of the RSPI can be summarized as:

$$\Delta\tilde{\pmb{u}}_{PI} = \sum\Delta\tilde{\pmb{u}}_S^i. \tag{49}$$

3.4 Sensor Data Processing
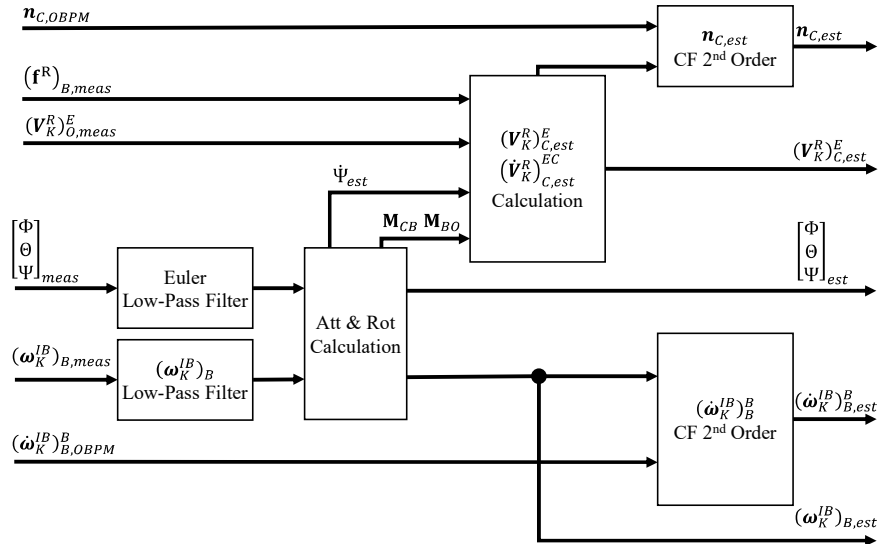
Fig. 6 Scheme of the Estimator in the Flight Control System

In the realm of simulating real-world phenomena, the nonlinear simulations incorporate realistic sensor behaviour. This realism encompasses factors such as bias, stochastic noise, nonlinearity, and temperature effects. Considering the sensors available on the aircraft, which track attitudes, rotational speeds, and accelerations, it becomes evident that measurements require filtering and data estimation (e.g., rotational acceleration, as seen in Eq. (15)). This section delves into the workings of the estimator, which employs different types of filters, as illustrated in Fig. 6. Real-world measurements invariably contain noise. A

common step involves passing the measurements through a low-pass filter with a cutoff frequency denoted as ω_0 and a relative damping factor ζ. The transfer function of a second-order low-pass filter can be expressed as [25]:

$$G_{LP}(s) = \frac{\omega_0^2}{s^2 + 2\zeta\omega_0 s + \omega_0^2}.$$

(50)

Eq. (50) introduces additional time delays into the system's feedback loop. A complementary filter (CF) is implemented, tasked with estimating the pseudo controls defined in Eq. (15). To illustrate, let's consider the estimation of the aircraft's rotational acceleration, denoted as $\hat{\dot{\omega}}$. This parameter cannot be directly measured by any sensor within the system. Following the principles outlined in [26], a CF is implemented, as depicted in Fig. 7.

Fig. 7 Complementary Filter of the Angular Acceleration

The estimated output of one element of the complementary filter can be described as:

$$\hat{Y}(s) = sG_{LP}(s)U_1(s) + \left(1 - G_{LP}(s)\right)U_2(s).$$

(51)

Eq. (51) includes the second-order low-pass filter from Eq. (50). The first part of the equation $sG_{LP}(s)U_1(s)$ includes a derivation of y and the lowpass part of the signal, while the second part $(1 - G_{LP}(s))U_2(s)$ describes the high-pass part of $\dot{y}$. Consider the signal y processes one element of the measurements of the angular velocity $\hat{\omega}$ and $\dot{y}$ from the angular accelerations $\hat{\dot{\omega}}_{OBPM}$ estimated from the OBPM. By use of the CF, the resulting is the estimated angular acceleration $\hat{\dot{\omega}}$. Discrete-time processing is facilitated using the MATLAB function c2d. During estimator initialization, the CF is configured as a state-space representation, utilizing inputs from measurements and the OBPM. The output is the estimated angular acceleration, defined by the state-space equations:

$$x_{k+1} = \Phi_k x_k + B_k u_k,$$

(52)

$$y_k = C_k x_k + D u_k,$$

(53)

with state matrix Φ, input matrix B, output matrix C, feedforward matrix D, the state vector x and the input vector u. The current vector is donated by the index k and next state accordingly by $k+1$ with respect to the sample time T. In this use case, the input and output vectors are:
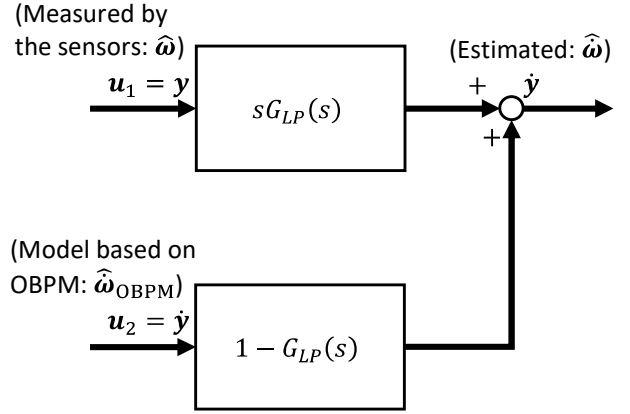
$$u = \begin{bmatrix} \hat{\omega} \\ \hat{\dot{\omega}}_{OBPM} \end{bmatrix},$$

(54)

$$y = \begin{bmatrix} \hat{\dot{\omega}} \end{bmatrix}.$$

Velocity and acceleration estimation is achieved through the equations:

$$(V_K^R)_C^E = M_{CO}(V_K^R)_O^E,$$

(55)

$$\left(\dot{V}_K^R\right)_C^{EC} = M_{CB}n_B - [((\omega_K^{OC})_C - M_{CB}(\omega_K^{IB})_B) \times (V_K^R)_C^E].$$

(56)

Eq. (55) and (56) involve various transformation matrices denoted by $\mathbf{M}$. $(\boldsymbol{\omega}_K^{OC})_C$ simplifies to $[0\ 0\ \Psi]^T$. The comprehensive filter settings are summarized in Table 4.

Table 4 Filter Settings of the Estimator

	Euler Low-Pass Filter	$(\boldsymbol{\omega}_K^{IB})_B$ Low-Pass Filter	$\boldsymbol{n}_C$ Complementary Filter	$(\dot{\boldsymbol{\omega}}_K^{IB})_B^B$ Complementary Filter
Cut-Off Frequency $\omega_0\ [rad/s]$	25	25	15	15
Damping ζ	1	1	1	1

4   Analysis and Simulation
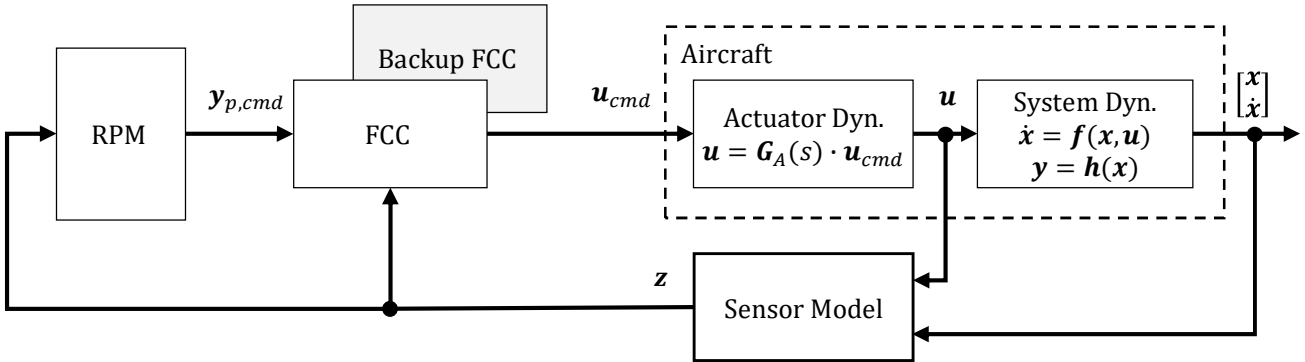
Fig. 8 System Simulation

Simulations are conducted with reference to Fig. 8, which depicts an integrated system involving a reactive pilot model (RPM), the flight control computer (FCC), aircraft dynamics with actuator behaviour, and a sensor model replicating real-world phenomena. The RPM embodies a logic model that computes controller commands based on the current flight phase, as detailed in [27]. In the actual hardware configuration, both a primary and backup FCC will be present. However, for this simulation, it is assumed that the hardware operates optimally, excluding the need for a backup system. The FCC runs with 250 Hz, each 0.004 s respectively. Additionally, time delays are conducted that account for process delays for the FCC output, the actuator responses, and the sensor outputs. The delays are characterized by 4 samples, which showcases a time delay of 0.016 s. The execution of the FCC and the filters is discrete, while the FDM runs in continuous execution.

4.1.1   Linear Uncertainty Analysis

Before delving into the assessment of nonlinear simulations, it is imperative to address real-world phenomena, such as biases inherent in the modelled system, to underscore the robustness of the INDI methodology. To achieve this, a previous example from [28] is utilized to evaluate the open loop gain and phase margin of the linear system, as traditionally accommodated in classical control theory. Leveraging Eq. (20), the ideal solution is derived from a perfect twin modelled within the OBPM framework, yielding the output $\hat{\mathbf{B}}_v$. However, in practical implementations, deviations occur due to the intricate nature of aircraft aerodynamics and propulsion representations. Particularly, eVTOL aircraft with tilt mechanisms and varying flight phases encounter complex airflow conditions. Consequently, elements of the effectiveness matrix may be over- or underestimated, thereby implying higher or lower effectiveness assumed by the OBPM.

If an element of the $\widehat{\mathbf{B}}_v$ is assumed to be:

$$b_{m,n} = \frac{\delta v_m}{\delta u_n}, \tag{57}$$

with the m-th pseudo control and n-th effector, an imperial manipulation of the element with Δb_{uncert} can be expressed as:

$$b_{m,n}^* = \frac{\delta v_m}{\delta u_n} + \Delta b_{uncert}. \tag{58}$$

The uncertainty factor is then:

$$\gamma = \frac{b_{m,n}}{b_{m,n} + \Delta b_{uncert}}. \tag{59}$$

The factor γ shows the derivation from the ideal model. Under consideration of Eq. (20), back transformation to $\Delta \boldsymbol{v}_{des} = \mathbf{B}_v \Delta \boldsymbol{u}$ can be used to identify the effector exerting the most significant influence on the pseudo controls. During hover, the propulsion systems, and during wingborne flight, the aerodynamic surfaces, stand out as the primary contributors to the pseudo controls, consequently resulting in the highest impact on uncertainties.

In the linear analysis, γ is varied within a range of -0.3 to +0.3, representing uncertainties of up to +/- 30% in the elements of both propulsion and aerodynamic surfaces. As illustrated in Fig. 9, this analysis provides insights into the gain and phase margins of the inner loop pseudo control of the roll axis. Both, hover and wingborne scenarios exhibit a consistent trend: increased gain and phase margins for positive uncertainties, and decreased margins for negative uncertainties.

Positive uncertainties indicate overestimations of the effectors, resulting in smaller control increments as per Eq. (20). This slower convergence to the desired trajectory necessitates increasing gains in the EC, rendering the system more sensitive to sensor noise. Conversely, underestimation amplifies the control allocation solution, leading to a higher loop gain. If the OBPM model is underestimated, the desired incremental solution may lead to incremental saturations, adversely affecting the aircraft behaviour.

Nevertheless, despite these uncertainties, the system demonstrates robustness, maintaining stable in the frequency domain in hover and wingborne conditions.
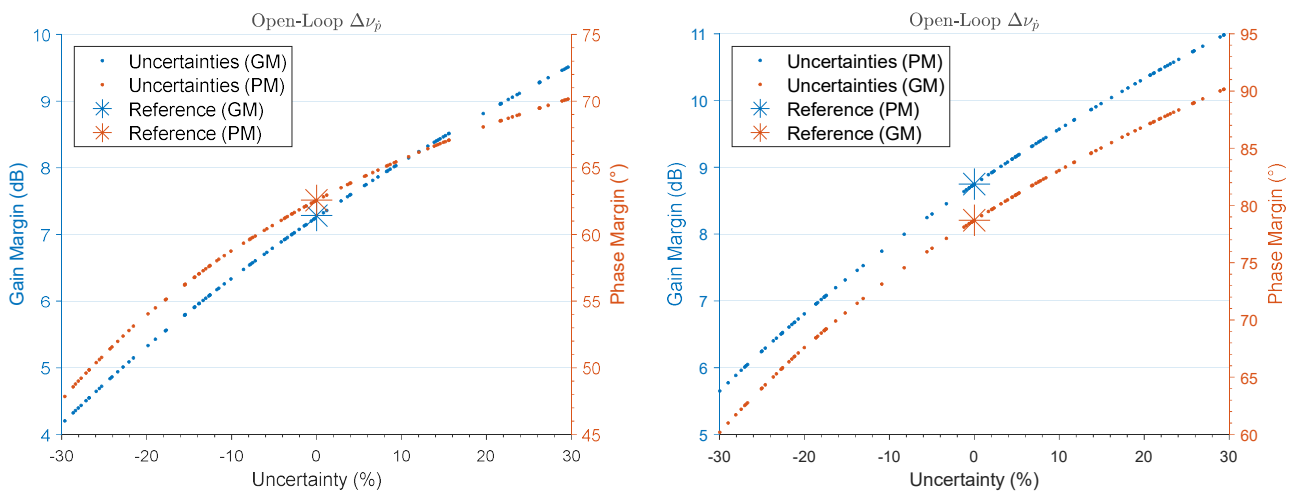
Fig. 9 Open-Loop Gain and Phase Margin with Uncertainties - left: Hover, right: Wingborne

4.1.2 Nonlinear Simulations

For the conducted nonlinear simulations in this paper, a brief mission is presented, illustrating precise tracking of pseudo controls by the angular acceleration, as shown in Fig. 13, and the load factors in the C-frame, displayed in Fig. 14. The flight profile comprises hovering, wingborne flight, and transition. The aircraft initiates by hovering and gradually gains altitude and moving sideways. Subsequently, the eVTOL accelerates into wingborne flight, executes manoeuvres, and then decelerates back into hover as shown in Fig. 10. The simulated environment includes a rotating spherical world and realistic sensor behaviour. The primary focus is on evaluating the FCC performance for accurate control and data filtering, particularly in the presence of noisy measurements. Additionally, all actuator and propulsion efficiencies are manipulated by an underestimation of 15 % to account for uncertainties.
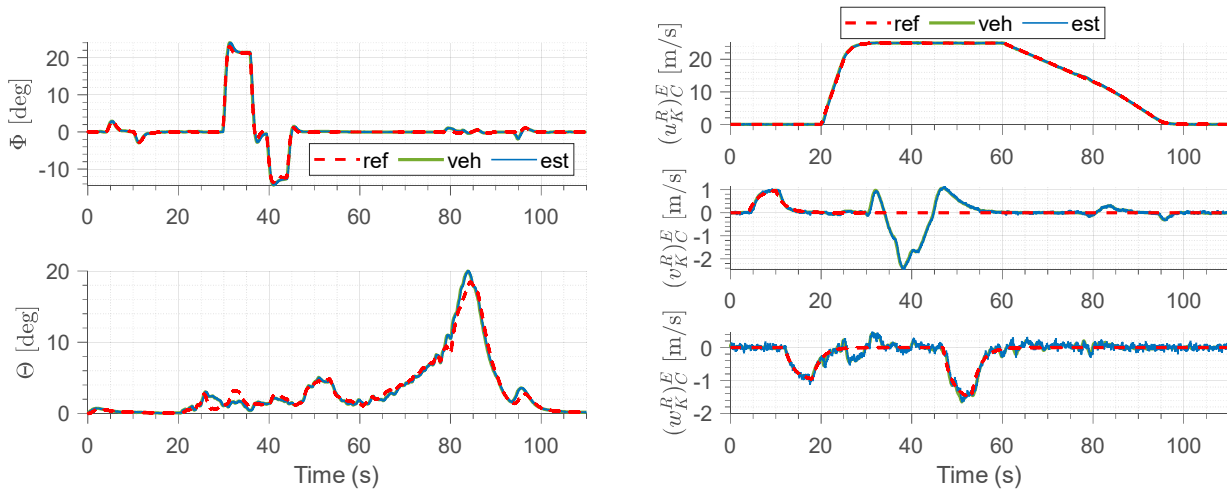
Fig. 10 Attitude and Velocity Tracking

Fig. 13 illustrates the estimation of angular accelerations, showcasing satisfactory tracking. The estimation coverage is highlighted in blue, while the real vehicle states are depicted in green. The dashed red line represents commands from the RM. Despite minor oscillations during the transition with acceleration and deceleration around 22 s and 76 s, respectively, the control system adeptly tracks the desired trajectory. Particularly noteworthy is the good tracking performance of RM inputs during hover until 20 s.

The tracking of load factors in the C-frame, as depicted in Fig. 14, also demonstrates accurate tracking. The overshoot of acceleration during transition to wingborne flight at 20 s is rapidly attenuated due to aircraft inertia. Larger oscillations in measurements are generally observed in wingborne flight, attributed to faster translation tracked solely by the GPS system with lower measurement rates. However, the estimator effectively eliminates noise and closely tracks the load factors, aligning well with real vehicle data in blue.

Notably, there are brief deviations in desired altitude, represented by vertical load factor, during transitions between hover and wingborne flight (at 24 s and 80 s). Especially during the forward transition, the aircraft increases its altitude, as shown in Fig. 10. However, the eVTOL returns to the desired altitude by reducing the vertical velocity according to the reference model, thereby maintaining the desired altitude. This transitional phase highlights changes in the effectiveness of propulsion and aerodynamic surfaces, as well as lift generation. Nonetheless, altitude is swiftly regained, and full control authority is restored.

With regards to the actuators illustrated in Fig. 15, it is notable that the front propellers are shut down during transition, while the tilt of the propulsion accounts for acceleration. A positive consequence of this

is the maintenance of a pitch angle above zero degrees throughout the transition, ensuring positive lift. Additionally, the flaps move to 5 degrees until achieving wingborne flight as per desired constraints. The interplay between propulsion and aerodynamic surfaces during transition can be observed, with acceptable coordination. Particularly during the back-transitioning at 82 s, the ruddervator generates a pitch-up moment while the tilt deflections of the front propellers increase beforehand. This behaviour underscores the challenge of balancing constraints and the effects of varying effectiveness.

Finally, Fig. 11 and Fig. 12 demonstrate the effects of the control allocation extensions as previously described. The numerical robustness of the inverse of $\hat{\mathbf{B}}_\nu$ is notably improved by a factor of 10^3 compared to a standard CA with respect to the condition. This enhancement greatly improves robustness, facilitating a more efficient utilization of the most effective effectors. During transition, RSPI iteration is most pronounced, reaching a maximum of 2 iterations. This could be attributed to high gains in the EC or a rapid RM. The CA tries to find the best fit for the pseudo control, while it computes the reached pseudo controls by taking Eq. (47) into account. However, overall system performance remains moderate, necessitating only minor adjustments.
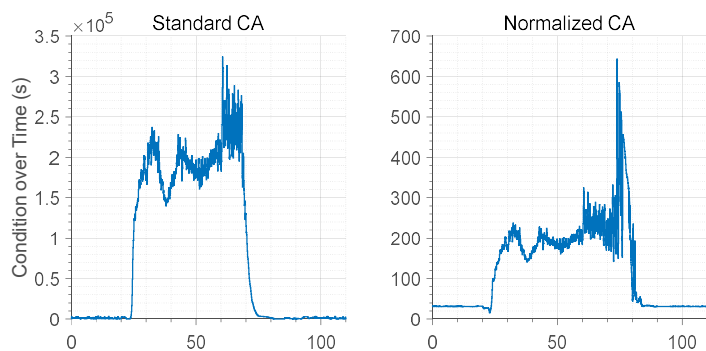
Fig. 11 Condition of Standard and Normalized Control Allocation
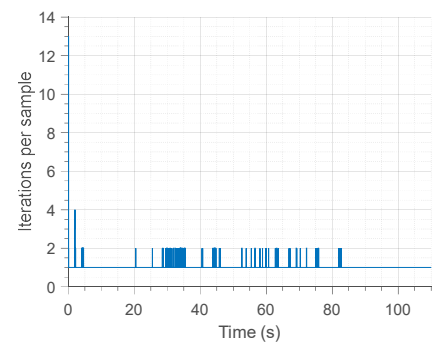
Fig. 12 Number of Iterations within the RPSI

5 Conclusion

In this paper, an incremental nonlinear dynamic inversion (INDI) approach for the flight control system (FCS) of a conceptual aerial vehicle, particularly focusing on an electrical vertical take-off and landing (eVTOL) configuration is presented. The implementation of INDI addresses the challenges associated with an over-actuated system, providing effective control across various flight phases. In addition, control allocation methods and the incorporation of a redistributed scaled pseudo inverse (RSPI) to enhance control precision is applied. The significance of sensor data processing and estimation techniques, crucial for achieving accurate control in real-world scenarios, is presented. Especially the complementary filter (CF) of the angular acceleration is pointed out. The INDI control is evaluated in the linear system with uncertainties for the hover and wingborne case. The linear evaluation shows robustness against uncertainties.

The nonlinear simulations, containing a 6-DOF model, actuator and sensor models, a reactive pilot model (RPM), and the flight control computer (FCC), conducted demonstrate the viability and efficacy of the proposed methodologies, showcasing precise pseudo control. The results underscore the importance of accurate control and data filtering, laying the foundation for further research and development in this domain. Despite a 15% underestimation in the effectiveness of system elements, the simulation remains stable and exhibits satisfactory performance.
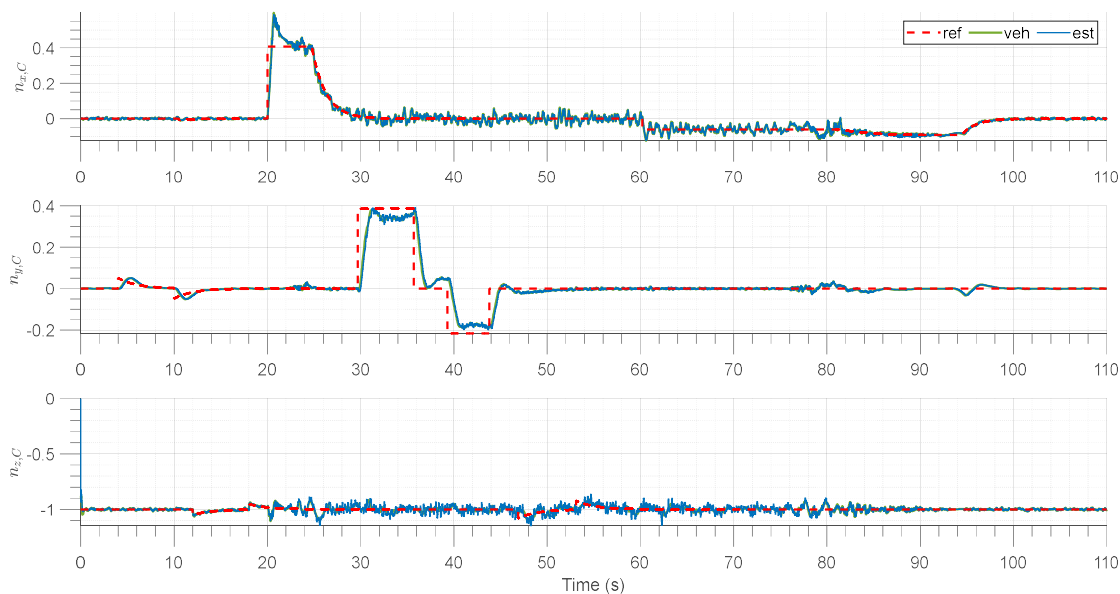
Overall, this research contributes to advancing the understanding of control strategies for eVTOL vehicles, setting the stage for future investigations into system integration with backup FCC for hardware-in-the-loop (HIL) testing.
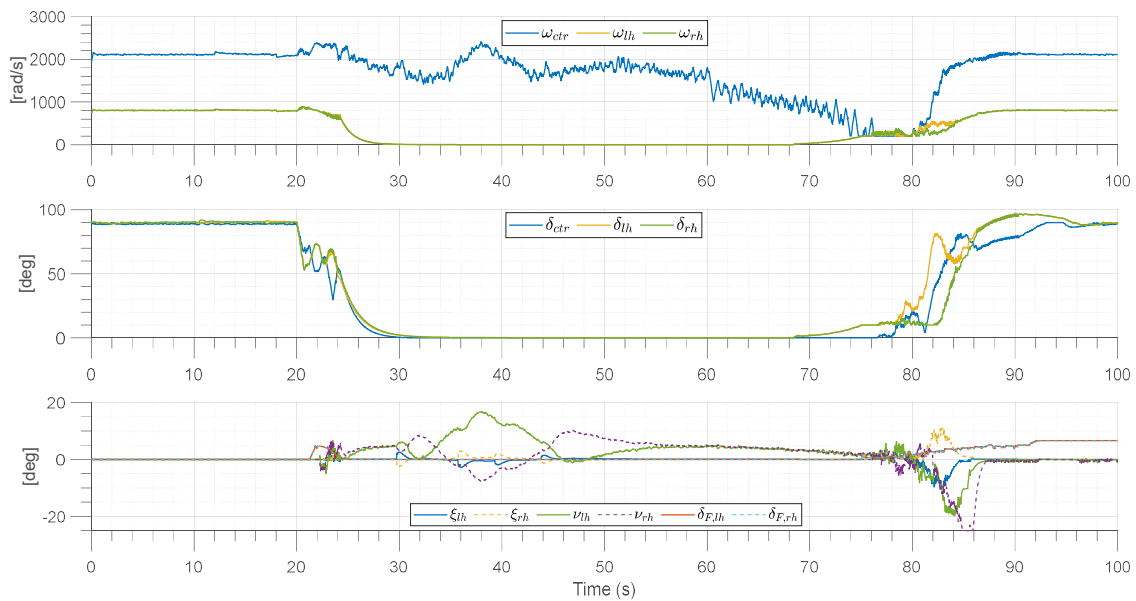
Acknowledgments
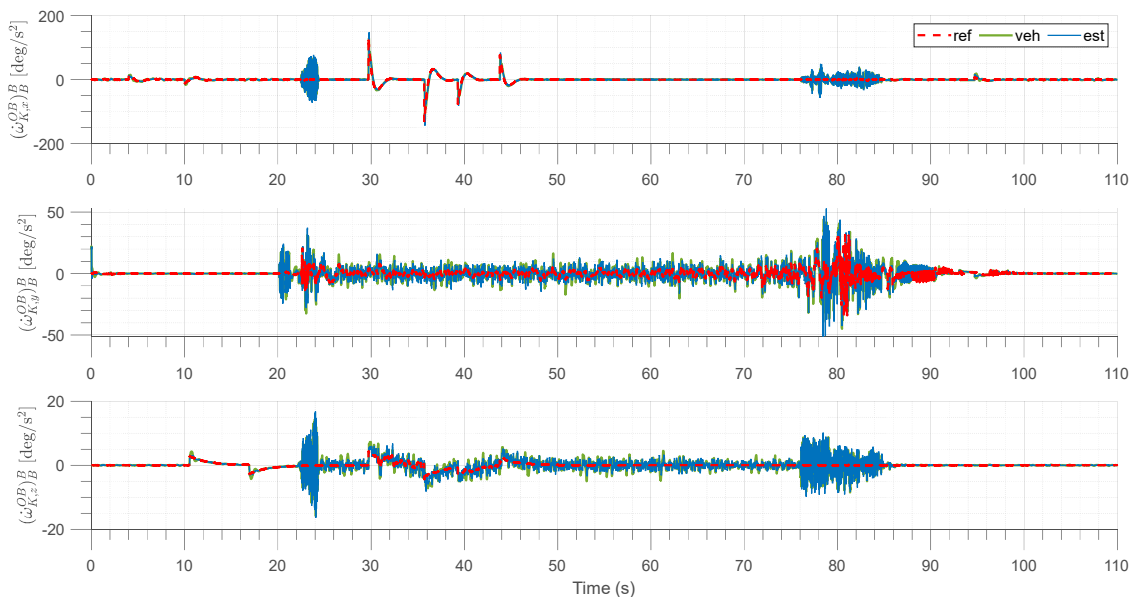
Fig. 13 Rotational Acceleration of the Nonlinear Simulations

Fig. 14 Load Factor of the Nonlinear Simulation

Fig. 15 Actuator Tracking

6 References

[1] Whitney, J., "URBAN AIR MOBILITY," *Military & Aerospace Electronics*, Vol. 34, No. 2. 1 Jan. 2023, URL: https://www.militaryaerospace.com/magazine/62270 [retrieved 7 August 2023].

[2] Sigari, C., and Biberthaler, P., "Medizinische Drohnen: innovative Technologie eröffnet neue Horizonte der Unfallchirurgie," *Der Unfallchirurg*, Vol. 124, No. 12. 2021, pp. 974–976. doi: 10.1007/s00113-021-01095-3.

[3] Garnica-Peña, R. J., and Alcántara-Ayala, I., "The use of UAVs for landslide disaster risk research and disaster risk management: a literature review," *Journal of Mountain Science*, Vol. 18, No. 2. 2021, pp. 482–498.
doi: 10.1007/s11629-020-6467-7.

[4] Myschik, S., Kinast, L., Huemer, M., Vicca, D., Dollinger, D., et al., "Development of a Flight Control System for a Cyclocopter UAV Demonstrator," *AIAA AVIATION 2022 Forum,* American Institute of Aeronautics and Astronautics, Chicago, IL & Virtual. 2022.

[5] Lombaerts, T., van Schravendijk, M., Chu, P., and Mulder, J. A., "Adaptive Nonlinear Flight Control and Control Allocation for Failure Resilience," *Advances in Aerospace Guidance, Navigation and Control,* edited by F. Holzapfel and S. Theil, Springer Berlin Heidelberg, Berlin, Heidelberg. 2011, pp. 41–53.

[6] Snell, S. A., Enns, D. F., and Garrard, W. L., "Nonlinear inversion flight control for a supermaneuverable aircraft," *Journal of Guidance, Control, and Dynamics*, Vol. 15, No. 4. 1992, pp. 976–984.
doi: 10.2514/3.20932.

[7] Brockhaus, R., Alles, W., and Luckner, R., *Flugregelung,* Springer, Berlin, Heidelberg. 2011.

[8] "Aircraft Control and Simulation Dynamics Controls Design and Autonomous Systems - 2015 - Stevens,".

[9] *Flight dynamic principles. A linear systems approach to aircraft stability and control,* Butterworth-Heinemann, Amsterdam. 2007.

[10] Hoerner, S. F., and Borst, H. V., *Fluid-dynamic lift: practical information on aerodynamic and hydrodynamic lift*. 1975.

[11] Lombaerts, T., Kaneshige, J., Schuet, S., Aponso, B. L., Shish, K. H., et al., "Dynamic Inversion based Full Envelope Flight Control for an eVTOL Vehicle using a Unified Framework," *AIAA Scitech 2020 Forum,* American Institute of Aeronautics and Astronautics, Orlando, FL, USA. 2020.

[12] Quan, Q., *Introduction to Multicopter Design and Control,* Springer Singapore, Singapore. 2017.

[13] Surmann, D., Zrenner, M., and Myschik, S., "Flight Performance Evaluation of a Conceptual eVTOL System using Nonlinear Simulations," *AIAA SCITECH 2022 Forum,* American Institute of Aeronautics and Astronautics, San Diego, CA, USA. 2022.

[14] Bhardwaj, P., Raab, S. A., Zhang, J., and Holzapfel, F., "Thrust command based Integrated Reference Model with Envelope Protections for Tilt-rotor VTOL Transition UAV," *AIAA Aviation 2019 Forum,* American Institute of Aeronautics and Astronautics, Dallas, TX, USA. 2019.

[15] Bhardwaj, P., Raab, S. A., Zhang, J., and Holzapfel, F., "Integrated Reference Model for a Tilt-rotor Vertical Take-off and Landing Transition UAV," *2018 Applied Aerodynamics Conference,* American Institute of Aeronautics and Astronautics, Atlanta, GA, USA. 2018.

[16] Surmann, D., and Myschik, S., "Gain Design of an INDI-based Controller for a Conceptual eVTOL in a Nonlinear Simulation Environment," *AIAA SCITECH 2023 Forum,* American Institute of Aeronautics and Astronautics, National Harbor, MD & Online. 2023.

[17] Zhang, J., Wang, J., Zhang, F., and Holzapfel, F., "Modeling and Incremental Nonlinear Dynamic Inversion Control for a Highly Redundant Flight System," *AIAA Scitech 2019 Forum,* American Institute of Aeronautics and Astronautics, San Diego, CA, USA. 2019.

[18] Johansen, T. A., and Fossen, T. I., "Control allocation—A survey," *Automatica*, Vol. 49, No. 5. 2013, pp. 1087–1103. doi: 10.1016/j.automatica.2013.01.035.

[19] Durham, W., Bordignon, K. A., and Beck, R., *Aircraft control allocation,* Wiley, Chichester West Sussex United Kingdom. 2017.

[20] Sieberling, S., Chu, Q. P., and Mulder, J. A., "Robust Flight Control Using Incremental Nonlinear Dynamic Inversion and Angular Acceleration Prediction," *Journal of Guidance, Control, and Dynamics*, Vol. 33, No. 6. 2010, pp. 1732–1742. doi: 10.2514/1.49978.

[21] Smith, P., "A simplified approach to nonlinear dynamic inversion based flight control," *23rd Atmospheric Flight Mechanics Conference,* American Institute of Aeronautics and Astronautics, Boston, MA, USA. 1998.

[22] Zhang, J., Bhardwaj, P., Raab, S. A., Saboo, S., and Holzapfel, F., "Control Allocation Framework for a Tilt-rotor Vertical Take-off and Landing Transition Aircraft Configuration," *2018 Applied Aerodynamics Conference,* American Institute of Aeronautics and Astronautics, Atlanta, GA, USA. 2018.

[23] Zhang, J., Bhardwaj, P., Raab, S. A., and Holzapfel, F., "Control Allocation Framework with SVD-based Protection for a Tilt-rotor VTOL Transition Air Vehicle," *AIAA Aviation 2019 Forum,* American Institute of Aeronautics and Astronautics, Dallas, TX, USA. 2019.

[24] Surmann, D., Hein, L., and Myschik, S., "Control Allocation Methoden zur nichtlinearen Regelung eines elektrischen Transitionsvehikels," *Deutscher Luft- und Raumfahrtkongress 2022,* Dresden, Germany. 2022.

[25] Skogestad, S., and Postlethwaite, I., *Multivariable feedback control. Analysis and design,* 2nd ed., Wiley, Chichester. 2010.

[26] Steffensen, R., Steinert, A., Mbikayi, Z., Raab, S., Angelov, J., et al., "Filter and sensor delay synchronization in incremental flight control laws," *Aerospace Systems.* 2023. doi: 10.1007/s42401-022-00186-2.

[27] Surmann, D., Sauert, N., Hein, L., and Myschik, S., "Reactive Pilot Model Design for Automatic Mission Simulation of a Transition Vehicle," *AIAA AVIATION 2023 Forum,* American Institute of Aeronautics and Astronautics, San Diego, CA and Online. 2023.

[28] Surmann, D., Panchal, P., and Myschik, S., "Integrated Flight Control System Architecture and Robustness Analysis for a Lift-to-Cruise Aircraft with Incremental Nonlinear Dynamic Inversion," *Vertical Flight Society 80th Annual Forum & Technology Display,* Vertical Flight Society 80th Annual Forum & Technology Display, Montréal, Québec, Canada. 2024, pp. 1–14.